agriculture

MDPI

Article

Surface Soil Moisture Estimation Taking into Account the Land Use and Fractional Vegetation Cover by Multi-Source Remote Sensing

Rencai Lin [1,2,3], Xiaohua Xu [1,2,3,*], Xiuping Zhang [1,2,3], Zhenning Hu [4], Guobin Wang [1,2,3], Yanping Shi [1,2,3], Xinyu Zhao [5] and Honghui Sang [5]

[1] Jiangxi Academy of Water Science and Engineering, Nanchang 330029, China; rencaihrs@iwhr.com (R.L.); rainaleaf@163.com (X.Z.); wgb_jx@163.com (G.W.); 2020301014@nit.edu.cn (Y.S.)
[2] Jiangxi Province Key Laboratory of Flood and Drought Disaster Prevention, Nanchang 330029, China
[3] Jiangxi Provincial Technology Innovation Center for Ecological Water Engineering in Poyang Lake Basin, Nanchang 330029, China
[4] School of Water Conservancy and Transportation, Zhengzhou University, Zhengzhou 450001, China; hzn999@gs.zzu.edu.cn
[5] School of Soil and Water Conservation, Nanchang Institute of Technology, Nanchang 330099, China; spxyz@nit.edu.cn (X.Z.); 2022994876@nit.edu.cn (H.S.)
* Correspondence: zgxxh79@163.com

Abstract: Surface soil moisture (SSM) plays a pivotal role various fields, including agriculture, hydrology, water environment, and meteorology. To investigate the impact of land use types and fractional vegetation cover (FVC) on the accuracy of SSM estimation, this study conducted a comprehensive analysis of SSM estimation performance across diverse land use scenarios (e.g., multiple land use combinations and cropland) and varying FVC conditions. Sentinel-2 NDVI and MOD09A1 NDVI were fused by the Enhanced Spatial and Temporal Adaptive Reflection Fusion Model (ESTARFM) to obtain NDVI with a temporal resolution better than 8 d and a spatial resolution of 20 m, which improved the matching degree between NDVI and the Sentinel-1 backscattering coefficient (σ^0). Based on the σ^0, NDVI, and in situ SSM, combined with the water cloud model (WCM), the SSM estimation model is established, and the model of each land use and FVC is validated. The model has been applied in Handan. The results are as follows: (1) Compared with vertical–horizontal (VH) polarization, vertical–vertical (VV) polarization is more sensitive to soil backscattering (σ^0_{soil}). In the model for multiple land use combinations (Multiple-Model) and the model for the cropland (Cropland-Model), the R^2 increases by 0.084 and 0.041, respectively. (2) The estimation accuracy of SSM for the Multiple-Model and Cropland-Model is satisfactory (Multiple-Model, RMSE = 0.024 cm^3/cm^3, MAE = 0.019 cm^3/cm^3, R^2 = 0.891; Cropland-Model, RMSE = 0.023 cm^3/cm^3, MAE = 0.018 cm^3/cm^3, R^2 = 0.886). (3) When the FVC > 0.75, the accuracy of SSM by the WCM is low. It is suggested the model should be applied to the cropland where the FVC $\leq$ 0.75. This study clarified the applicability of SSM estimation by microwave remote sensing (RS) in different land uses and FVCs, which can provide scientific reference for regional agricultural irrigation and agricultural water resources management. The findings highlight that the VV polarization-based model significantly improves SSM estimation accuracy, particularly in croplands with FVC $\leq$ 0.75, offering a reliable tool for optimizing irrigation schedules and enhancing water use efficiency in agriculture. These results can aid in better water resource management, especially in regions with limited water availability, by providing precise soil moisture data for informed decision-making.

check for updates

Academic Editor: Alessandro D'Emilio

Received: 13 January 2025
Revised: 22 February 2025
Accepted: 24 February 2025
Published: 25 February 2025

Citation: Lin, R.; Xu, X.; Zhang, X.; Hu, Z.; Wang, G.; Shi, Y.; Zhao, X.; Sang, H. Surface Soil Moisture Estimation Taking into Account the Land Use and Fractional Vegetation Cover by Multi-Source Remote Sensing. *Agriculture* **2025**, *15*, 497. https://doi.org/10.3390/agriculture15050497

Copyright: © 2025 by the authors. Licensee MDPI, Basel, Switzerland. This article is an open access article distributed under the terms and conditions of the Creative Commons Attribution (CC BY) license (https://creativecommons.org/licenses/by/4.0/).

Keywords: water cloud model; Sentinel-1; NDVI; ESTARFM; vegetation water content

1. Introduction

Soil moisture (SM) is an important variable in the fields of agriculture, meteorology, and hydrology [1]. It is widely used in water resources evaluation, weather forecast, and hydrological simulation [2]. In the field of agriculture, the surface soil moisture (SSM) is one of the fundamental data for developing irrigation systems. Timely and accurate acquisition of SSM is of great significance for guiding agricultural irrigation and improving the utilization efficiency of agricultural water resources [3]. The in situ measurements of SSM include the drying method [4] and time domain reflectometry (TDR) [5]. These methods can obtain high time resolution and accurate SSM at the point scale, and are widely used in the validation of various SSM estimation models based on remote sensing (RS) [6]. At the same time, extensive manpower, materials, and financial resources need to be used, and regional-scale monitoring cannot be realized. With the advancement in RS technology, SSM monitoring at the regional scale has become feasible. The estimation accuracy of SSM has consistently improved as well, making it an essential tool for SSM monitoring at the regional scale. The Haihe basin is located in eastern China, including Beijing and Tianjin, which plays an important role in the politics and economy of China. The cropland in the basin accounts for 8% of the country, while water resources account for only 1.3% of the country [7]. Therefore, it is of great significance to study SSM in the Haihe basin, which can provide scientific reference for regional agricultural irrigation and agricultural water resources management.

The research on SSM monitoring at the regional scale using RS methods has achieved fruitful results. Scholars have proposed a series of SSM estimation models, such as empirical regression [8], water deficit index [9], water balance principle [10], and machine learning [11]. Lin et al. [12] carried out SSM estimation in the Hetao Irrigation District based on the crop water stress index (CWSI). Only monthly SSM was obtained with a spatial resolution of 250 m because of the lack of optical images. With the gradual development of microwave RS technology, researchers are more inclined to use microwave RS methods or the combination of microwave and optical RS to estimate SSM. Microwave RS is less affected by adverse weather such as clouds and rain. The microwave RS can be categorized into two types: active microwave and passive microwave RS. The spatial resolution of passive microwave RS is coarse, and its application in agriculture is limited. Active microwave RS has high spatial resolution, and its advantages in agriculture and hydrology are more obvious. Recent advancements in unmanned aerial vehicles (UAVs) have significantly enhanced agricultural monitoring capabilities, particularly in crop health assessment and SSM estimation [13,14]. UAVs offer high spatial and temporal resolution, making them suitable for precision agriculture [15]. However, challenges remain in integrating UAV data with other RS sources, especially in regions with complex land use and vegetation cover. Previous studies have primarily focused on single-source data, often neglecting the combined effects of land use and fractional vegetation cover (FVC) on SSM estimation. This study addresses these gaps by integrating multi-source RS data, including Sentinel-1 (S1) and Sentinel-2 (S2), to improve the accuracy of SSM estimation in the Haihe Basin, China. Many scholars have proposed a series of SSM estimation models in vegetated areas based on active microwave RS, such as the Alpha approximation model [16] and water cloud model (WCM) [17]. Existing methods may perform poorly under specific land types or FVC, or have limited accuracy under certain climatic conditions.

The WCM is a commonly used semi-empirical model for SSM estimation in vegetated areas based on active microwave RS [17]. The principle is that the total scattering is equal to the sum of vegetation backscattering (σ^0_{veg}), soil backscattering (σ^0_{soil}), and vegetation–soil multiple backscattering ($\sigma^0_{soil-veg}$) [18]. The $\sigma^0_{soil-veg}$ is usually neglected [19]. Therefore, the WCM fully integrates the advantages of multi-source RS and improves the estimation accuracy of SSM [20–22]. Gherboudj et al. [23] used Radarsat-2 data to perform SSM estimation in two cropland test areas, providing an RMSE of 0.059 and 0.066 cm^3/cm^3, respectively. Based on the WCM using fully polarized C-band and L-band data, Hosseini and McNairn [24] estimated SSM in a wheat field. The results showed L-band was more suitable for SSM estimation (the estimation accuracy of L-band, 0.064 cm^3/cm^3; the estimation accuracy of C-band, 0.078 cm^3/cm^3). Using S1, S2, and the WCM, Lin et al. [25] estimated the SSM in cropland located in Daxing and Gu'an. By incorporating the MCARI to enhance the WCM, they achieved highly promising results, with an R^2 of 0.867, an RMSE of 0.028 cm^3/cm^3, and a MAE of 0.023 cm^3/cm^3. Taking GF-3 and Landsat-8 as data sources, Zhang et al. [26] used the normalized difference infrared index (NDII) to characterize the VWC, and then used the WCM to estimate SSM. Bao et al. [27] compared the sensitivity of the NDVI, EVI, and NDWI to the VWC. The results showed that the NDWI had the best estimation accuracy of VWC, and the improved WCM was applied in Spain. Baghdadi et al. [28] used the NDVI to describe the VWC, and used the S1 and the WCM to estimate SSM in cropland and grassland. The results showed the VV polarization was more sensitive to the σ^0_{soil} when $0 < NDVI < 0.8$ and $0.05 < SSM < 0.35$ cm^3/cm^3.

Based on the identified research gaps, this study aims to address the following research questions: (1) How do different land use types and FVC affect the accuracy of SSM estimation using microwave RS? (2) What is the optimal combination of RS data (e.g., S1 and S2) and models (e.g., WCM) for accurate SSM estimation in agricultural regions? (3) Can the Enhanced Spatial and Temporal Adaptive Reflection Fusion Model (ESTARFM) improve the temporal and spatial resolution of NDVI, thereby enhancing the accuracy of SSM estimation?

Numerous scholars have extensively researched SSM estimation on polarization mode and RS data source. However, there is currently limited reporting on the influence of land uses and FVC on the accuracy of SSM estimation models in vegetated areas. Using the S1 and S2 of Area 1 from 1 January 2020 to 15 July 2021, the SSM estimation model was established based on the WCM to explore the differences in SSM estimation under different land use, and to propose the FVC range applicable to the WCM. All models are validated by the in situ SSM in Area 2 from 1 January 2020 to 15 July 2021. This study can provide scientific reference for guiding agricultural irrigation and improving the utilization efficiency of agricultural water resources.

2. Materials and Methodology

2.1. Study Area

The Haihe basin is located in eastern China, between 35°01′ N–42°45′ N and 111°57′ E–119°51′ E (Figure 1). The basin exhibits a distinct topographic gradient, with higher elevations in the northwest transitioning to lower elevations in the southeast, and is characterized by a pronounced monsoon climate. The region experiences an average annual temperature of approximately 10 °C, with an average annual precipitation of 500 mm. Precipitation patterns are highly variable, with approximately 80% of the annual rainfall occurring between May and October. The total area of the basin is 320,600 km^2, accounting for 3.3% of the total area of China. The basin belongs to the East Asian monsoon climate zone. Both Area 1 and Area 2 are rectangles measuring 185 km × 150 km. The SSM estimation models were established using in situ SSM data collected from Area 1, which

includes 31 SM monitoring sites. The models were then validated using independent in situ SSM data from Area 2, which includes 22 SSM monitoring sites. The validation process involved comparing the model-estimated SSM with the in situ SSM.

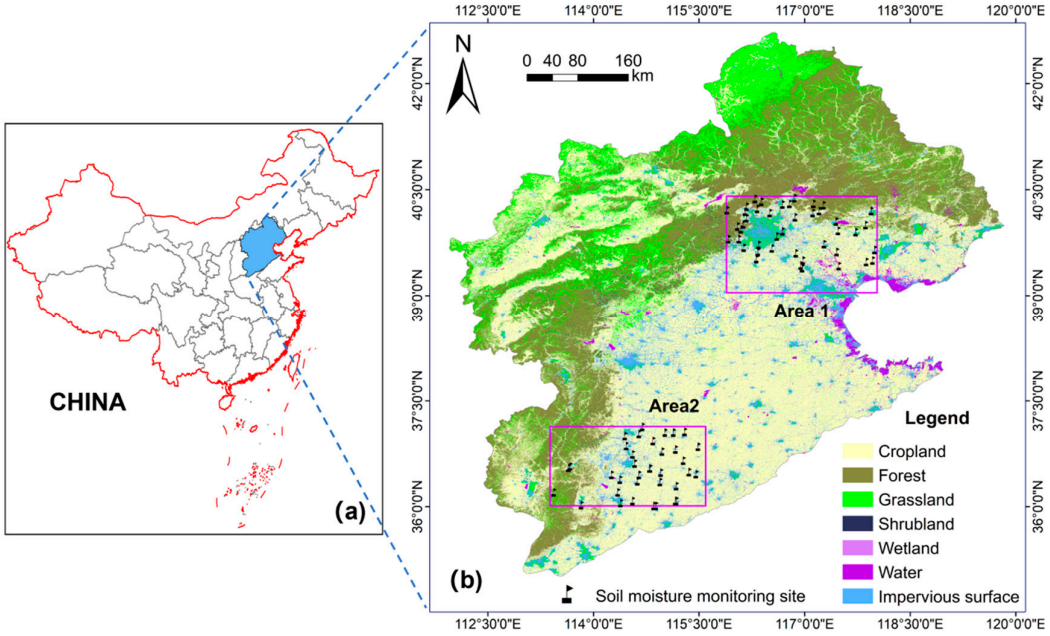


Figure 1. Distribution of SM observation sites and various land uses in the Haihe basin [29]. The in situ SSM in Area 1 is used for model construction, and the in situ SSM in Area 2 is used for validation. (**a**) map of China; (**b**) distribution of land use in Haihe Basin.

2.2. Data

2.2.1. Sentinel-1

S1 is a vital component of the European Earth Observation Copernicus Program, funded by the European Union. It includes two satellites (S1A and S1B), which were launched on 3 April 2014, and 25 April 2016, respectively. The time resolution of a single satellite is 12 d, which decreases to 6 d after two satellites are networked. The S1 is equipped with a C-band synthetic aperture radar (SAR) sensor and has a dual polarization mode, VV and VH, with a frequency of 5.4 GHz. The S1 data used in the research are Level 1-type products with ground range detection (GRD) from an interferometric wide (IW) mode. The S1 data were obtained during 1 January 2020 to 15 July 2021 from the website (https://search.asf.alaska.edu/#/, accessed on 1 October 2021). SARscape 5.2.3 was applied to conduct the radiometric calibration and geocoding to obtain the backscattering coefficient (σ^0). The backscatter radiation was calculated from previously calibrated S1 images and converted to decibels (db) by the transformation relation [30].

2.2.2. Sentinel-2

The Sentinel-2 mission comprises two satellites, S2A and S2B, each equipped with a multi-spectral imager capable of covering a swath width of 290 km. The S2A satellite is particularly notable for its advanced wide-swath high-resolution multi-spectral imager, which operates across 13 spectral bands. These bands are characterized by three distinct geometric resolutions, spanning from 10 to 60 m, enabling detailed and versatile remote sensing applications. With the launch of S2B, the two sensors in orbit have significantly shortened the revisit time, resulting in a 5 d interval for S2 images. Its superiority in spatiotemporal resolution provides adequate and high-quality data for many areas, facilitating the broad application of satellite images. The S2 images are provided freely for users through the United States Geological Survey (USGS) (https://glovis.usgs.gov/, accessed on 1 October

2021). The S2A images were obtained from 1 January 2020 to 15 July 2021, which period is close to those of the S1 images acquired. The S2 Level 1C images were selected, to which geometric and radiometric corrections were made. The Sentinel Application Platform (SNAP) was used to treat it as an L2A product.

2.2.3. MOD09A1

The MOD09A1 data were obtained from the standard land product captured by the MODIS (Moderate-Resolution Imaging Spectroradiometer) sensors (Irvine, CA, USA) aboard the Terra and Aqua satellites. The transit time of Terra is 10:30, and the transit time of Aqua is 13:30. The data used in this study are MOD09A1, and the acquisition time is from 1 January 2020 to 15 July 2021. MOD09A1 provides seven bands of Terra MODIS surface spectral reflectance with a spatial resolution of 500 m. The products can be downloaded from NASA (http://ladsweb.modaps.eosdis.nass.gov/, accessed on 1 October 2021); the MOD09A1 data have undergone radiometric calibration, atmospheric correction and geometric correction, reprojected to the WGS84/UTM coordinate system through the MODIS Reprojection Tool (MRT), and have quality control, data interpolation, and smoothing already performed [31] to provide the final band reflectance.

2.2.4. In Situ Surface Soil Moisture

A total of 53 SSM observation sites were strategically established across the study area, encompassing cropland, forest, and grassland. These sites were uniformly distributed throughout the Haihe basin to ensure representative coverage of different land use types. Daily SSM measurements were conducted at a depth of 10 cm from 1 January 2020 to 15 July 2021 (Figure 2). In situ SSM measurements were conducted using the method of Frequency Domain Reflectometry (FDR), which provide accurate and high-resolution SSM at point scale. SM was collected daily and recorded as volumetric water content (cm^3/cm^3). The FDR method was chosen due to its reliability and widespread use in SM studies, as it minimizes disturbances to the soil structure during measurement.

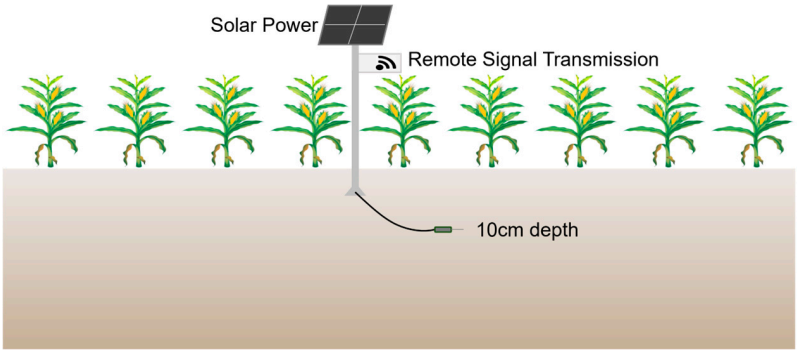


Figure 2. A sketch of the SM observation instrument.

2.3. Methodology

In this study, optical and microwave RS data were used to establish SSM estimation models under different land uses and FVCs based on the WCM, and the in situ SSM in Area 2 was used for validation. Figure 3 shows the flowchart for mapping SSM.

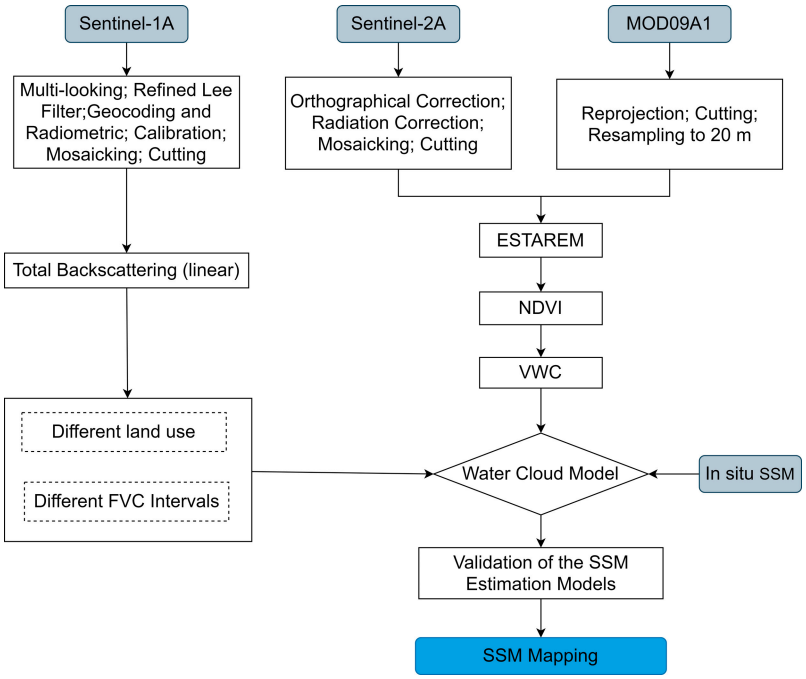


Figure 3. Flowchart for mapping SSM. Data sources include RS (i.e., S1, S2, and MOD09A1) and in situ SSM.

2.3.1. ESTARFM

Zhu et al. [32] proposed the ESTARFM, which can effectively complement the advantages of different RS data to generate images with appropriate spatiotemporal resolution. This method is applied to high-level RS data of different spatial resolutions, such as S2 NDVI and MODIS NDVI, with the purpose of realizing spatial downscaling of RS data from different levels and sources, so as to meet the demand of the NDVI with high spatiotemporal resolution in the study area. Figure 4 shows the date of MOD09A1 and S2 used, as well as the corresponding date in 2020 of data fusion. The calculation formulas for high spatial resolution images in the prediction period are as follows:

$$L_k(x_{w/2}, y_{w/2}, t_p) = L(x_{w/2}, y_{w/2}, t_k) + \sum_{i=1}^{N} W_i V_i \left(M(x_i, y_i, t_p) - M(x_i, y_i, t_k)\right) \quad (k = m, n) \tag{1}$$

$$L(x_{w/2}, y_{w/2}, t_p) = T_m L_m(x_{w/2}, y_{w/2}, t_p) + T_n L_n(x_{w/2}, y_{w/2}, t_p) \tag{2}$$

$$T_k = \frac{1 \Big/ \left| \sum_{j=1}^{w} \sum_{i=1}^{w} M(x_i, y_i, t_k) - \sum_{j=1}^{w} \sum_{i=1}^{w} M(x_i, y_i, t_p) \right|}{\sum_{k=m,n} \left(1 \Big/ \left| \sum_{j=1}^{w} \sum_{i=1}^{w} M(x_i, y_i, t_k) - \sum_{j=1}^{w} \sum_{i=1}^{w} M(x_i, y_i, t_p) \right| \right)} \quad (k = m, n) \tag{3}$$

where w is the search window for similar pixels; $(x_{w/2}, y_{w/2})$ is the position of the central pixel; (x_i, y_i) is the ith similar pixel; $L(x_{w/2}, y_{w/2}, t_k)$ and $M(x_i, y_i, t_k)$ are the NDVI images of high and low spatial resolution in the k ($k = m, n$) period; $L_m(x_{w/2}, y_{w/2}, t_p)$ and $L_n(x_{w/2}, y_{w/2}, t_p)$ are the NDVI images with high spatial resolution for period t_p predicted by high and low spatial resolution images for periods t_m and t_n; $L(x_{w/2}, y_{w/2}, t_p)$ is the NDVI image with high spatial resolution in the prediction period. V_i is the conversion coefficient; T_m and T_n are the temporal weights between times t_m and t_n, respectively. W_i is the comprehensive weight factor, and its expressions can be found in [33].

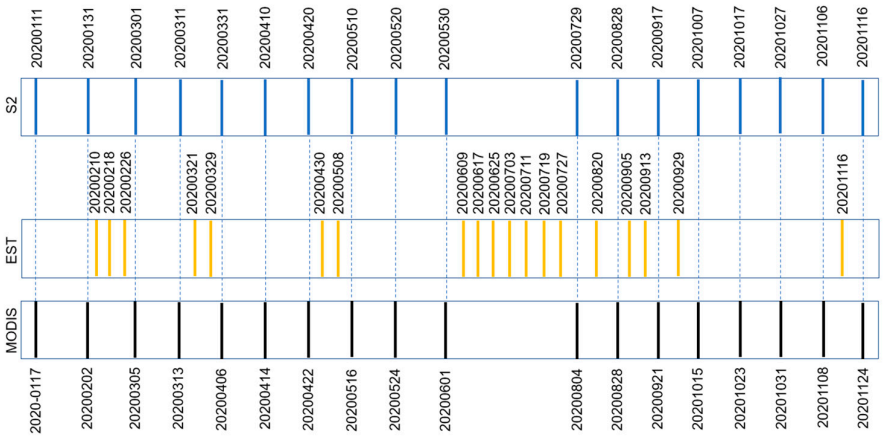


Figure 4. The use of MOD09A1 and S2, as well as the corresponding date of data fusion in 2020. For example, 2 February and 31 January 2020, and 5 March and 1 March 2020 are two pairs of coarse and fine spatial resolution data, which can be fused to obtain NDVI with a spatial resolution of 20 m in 10 February, 18 February, and 26 February 2020.

2.3.2. Water Cloud Model

To distinguish the soil backscattering (σ^0_{soil}) and vegetation backscattering (σ^0_{veg}) in the vegetated areas, the WCM developed by Attema and Ulaby [17] was adopted. The WCM is based on the radiative transfer model, assuming that the vegetation canopy is a uniform horizontal cloud layer, ignoring multiple scattering between the vegetation and the surface. The principle of the WCM is that the total scattering (σ^0) is equal to the sum of vegetation backscattering (σ^0_{veg}), soil backscattering (σ^0_{soil}), and vegetation–soil multiple backscattering ($\sigma^0_{\text{soil}-\text{veg}}$). $\sigma^0_{\text{soil}-\text{veg}}$ is usually neglected [19]. The model has the advantage of simplicity and practicality in describing radar-scattering mechanisms in vegetated areas. Thus, this model has often been used for relevant information estimation in vegetated areas. The WCM is expressed as follows:

$$\sigma^0 = \sigma^0_{veg} + T^2\sigma^0_{soil} \tag{4}$$

$$\sigma^0_{veg} = A\mathrm{M_v}\cos\theta\left(1 - T^2\right) \tag{5}$$

$$T^2 = \exp(-2\mathrm{BM_v}\sec\theta) \tag{6}$$

In addition, the term $\exp(-2\mathrm{BM_v}\sec\theta)$ is described with the Taylor formula:

$$T^2 = \exp(-2\mathrm{BM_v}\sec\theta) = 1 - 2\mathrm{BM_v}\sec\theta + 2\mathrm{B}^2\mathrm{M_v}^2\sec^2\theta + \cdots \tag{7}$$

where σ^0 is the total backscattering coefficient, db; σ^0_{veg} is the vegetation backscattering coefficient, db; σ^0_{soil} is the soil backscattering coefficient, db; T^2 is the two-way attenuation factor; θ is the incident angle, °; and A and B are parameters that depend on the type of vegetation. The terrain in Area 1 is flat, so an average incidence angle was adopted. The average incidence angle was 38.84°. The vegetation parameters A and B were set to 0.0012 and 0.091, respectively [34], based on the characteristics of the main crops in the Haihe basin (summer maize and winter wheat). These parameters were chosen to minimize the error between the model-estimated SSM and the in situ SSM during the calibration process. $\mathrm{M_v}$ is the VWC, $\mathrm{kg/m^2}$. This study used S2 images with the same or similar transit time as the S1 satellite and less than 10% cloud cover to calculate the NDVI because of the difficulty

in obtaining the VWC at a regional scale. According to the piecewise function relationship between the VWC and NDVI [35], the VWC can be obtained as follows:

$$\mathrm{VWC} = \begin{cases} 1.9134\mathrm{NDVI}^2 - 0.3215\mathrm{NDVI} & 0.17 < \mathrm{NDVI} \leq 0.5 \\ 4.2857\mathrm{NDVI} - 1.5429 & \mathrm{NDVI} > 0.5 \\ 0 & \mathrm{NDVI} \leq 0.17 \end{cases} \tag{8}$$

$$\mathrm{NDVI} = \frac{R_{nir} - R_{red}}{R_{nir} + R_{red}} = \frac{R_{b8} - R_{b4}}{R_{b8} + R_{b4}} \tag{9}$$

where R_{nir} is the reflectance of the near-infrared band, R_{red} is the reflectance of the red band, and R_{bx} is the reflectance of the x-band of the S2.

In summary, σ^0_{soil} after removing the influence of vegetation can be obtained:

$$\sigma^0_{soil} = \frac{\sigma^0 - 0.0012 \times \mathrm{VWC} \cos\theta (1 - \exp(-2 \times 0.091 \times \mathrm{VWC} \times \sec\theta))}{\exp(-2 \times 0.091 \times \mathrm{VWC} \sec\theta)} \tag{10}$$

2.3.3. SSM Estimation Model

The σ^0 coefficient is sensitive to the surface dielectric constant and is closely related to SSM. Mattia et al. (2006) [36] has shown there is a good linear correlation between σ^0_{soil} and SSM. While this linear assumption simplifies the model and facilitates practical application, it may not fully capture the complex interactions between SM, surface roughness, and vegetation cover. Future studies could explore non-linear relationships or incorporate additional parameters to improve the model's accuracy under diverse environmental conditions. In this study, due to the limited measured parameters, a linear model was chosen. σ^0_{soil} can be expressed as follows:

$$\sigma^0_{soil} = d \cdot \mathrm{SSM} + e \tag{11}$$

where d and e are the soil parameters.

2.3.4. Fractional Vegetation Coverage

The relationship between FVC and NDVI exhibits a significant correlation. Typically, a direct conversion relationship is established between the two to extract FVC. In this study, a pixel decomposition model is employed to calculate FVC [37]:

$$\mathrm{FVC} = \frac{\mathrm{NDVI} - \mathrm{NDVI_{soil}}}{\mathrm{NDVI_{veg}} - \mathrm{NDVI_{soil}}} \tag{12}$$

where NDVI is the normalized difference vegetation index calculated by the band in S2 (Equation (9)); $\mathrm{NDVI_{soil}}$ is the NDVI corresponding to the bare surface, and the regional pixel value statistics are arranged from small to large. The first 5% corresponding value is $\mathrm{NDVI_{soil}}$. $\mathrm{NDVI_{veg}}$ is the NDVI corresponding to the approximate full vegetation coverage. The statistics of regional pixel values are arranged from small to large, and the first 95% corresponding value is $\mathrm{NDVI_{veg}}$. The FVC can be divided into four grades: high, mid-high, middle, and low [38] (Table 1).

Table 1. Classification of the fractional vegetation cover and its corresponding range of the fractional vegetation cover values.

Grade	FVCs	FVC Values
I	Low coverage	$0 < FVC < 0.45$
II	Middle coverage	$0.45 \leq FVC < 0.6$
III	Mid-high coverage	$0.6 \leq FVC < 0.75$
IV	High coverage	$0.75 \leq FVC < 1$

2.3.5. Evaluation Metrics

In this study, four evaluation metrics [determination coefficients (R^2), mean absolute error (MAE), root mean square error (RMSE), and mean square error (MSE)] were computed to quantify the model performance. R^2 indicates how well the model fits the observed data. The closer the value is to 1, the better the explanatory power of the model. RMSE represents the average deviation between the calculated value of the model and the observed value. The smaller the value, the higher the estimation accuracy of the model. MSE is the average of the squared error of the estimate. Similar to RMSE, the smaller the value, the higher the accuracy of the estimate of the model. MAE represents the average absolute deviation between the estimated value of the model and the actual observed value. The smaller the value, the higher the estimated accuracy of the model. The evaluation metrics are calculated as follows:

$$R^2 = \frac{\sum_{i=1}^{n} \left(S_i - \overline{S}\right)^2}{\sum_{i=1}^{n} \left(M_i - \overline{S}\right)^2} \tag{13}$$

$$MAE = \frac{1}{n}\sum_{i=1}^{n}|S_i - M_i| \tag{14}$$

$$RMSE = \sqrt{\frac{1}{n}\sum_{i=1}^{n}(S_i - M_i)^2} \tag{15}$$

$$MSE = \frac{1}{n}\sum_{i=1}^{n}(S_i - M_i)^2 \tag{16}$$

where n is the number of validation values during the day, and M_i and S_i are the in situ and estimated SSM, respectively.

3. Results

3.1. NDVI Fusion Results Based on the ESTARFM

To visually illustrate the texture details of the NDVI, a 1 km × 1 km sub-region in Area 1 was clipped for analysis. The sub-region contains a variety of land uses such as cropland and forest, which can be considered representative. Multi-source NDVI from 13 March, 22 April, 16 May, 1 June, 4 August, and 21 September 2020 were selected for spatial comparison and validation. Figure 5 shows the spatial distribution of multi-source NDVI (MODIS-NDVI, S2-NDVI, and EST-NDVI) on representative dates. Notably, the MODIS-NDVI, with a spatial resolution of 500 m, fails to capture detailed texture features. In contrast, both S2-NDVI and EST-NDVI, with a finer spatial resolution of 20 m × 20 m, effectively resolve spatial and texture details. The spatial comparison of S2-NDVI and EST-NDVI on 13 March, 22 April, 16 May, 1 June, 4 August, and 21 September 2020, reveal that EST-NDVI and S2-NDVI exhibit comparable spatial characteristics. As illustrated in Figure 5, the scatter plots of S2-NDVI and EST-NDVI pixel values predominantly align along the 1:1 line, indicating a strong correlation and satisfactory fitting performance. The

R^2 ranges from 0.806 to 0.957, while the MAE varies between 0.033 and 0.093. Additionally, the RMSE falls within the range of 0.045 to 0.121, and the MSE is observed to be between 0.002 and 0.014. On 4 August 2020, the scatter plot results of S2-NDVI and EST-NDVI were worse than those of the other five dates, with an R^2, MAE, MSE, and RMSE of 0.806, 0.093, 0.014, and 0.121, respectively. In conclusion, the ESTARFM can be used to integrate NDVI in the Haihe basin, makes full use of MODIS with a high temporal resolution of 8 d, and improves the temporal resolution of the NDVI with a spatial resolution of 20 m, which can be the basis for further improving the matching degree between NDVI and σ^0.

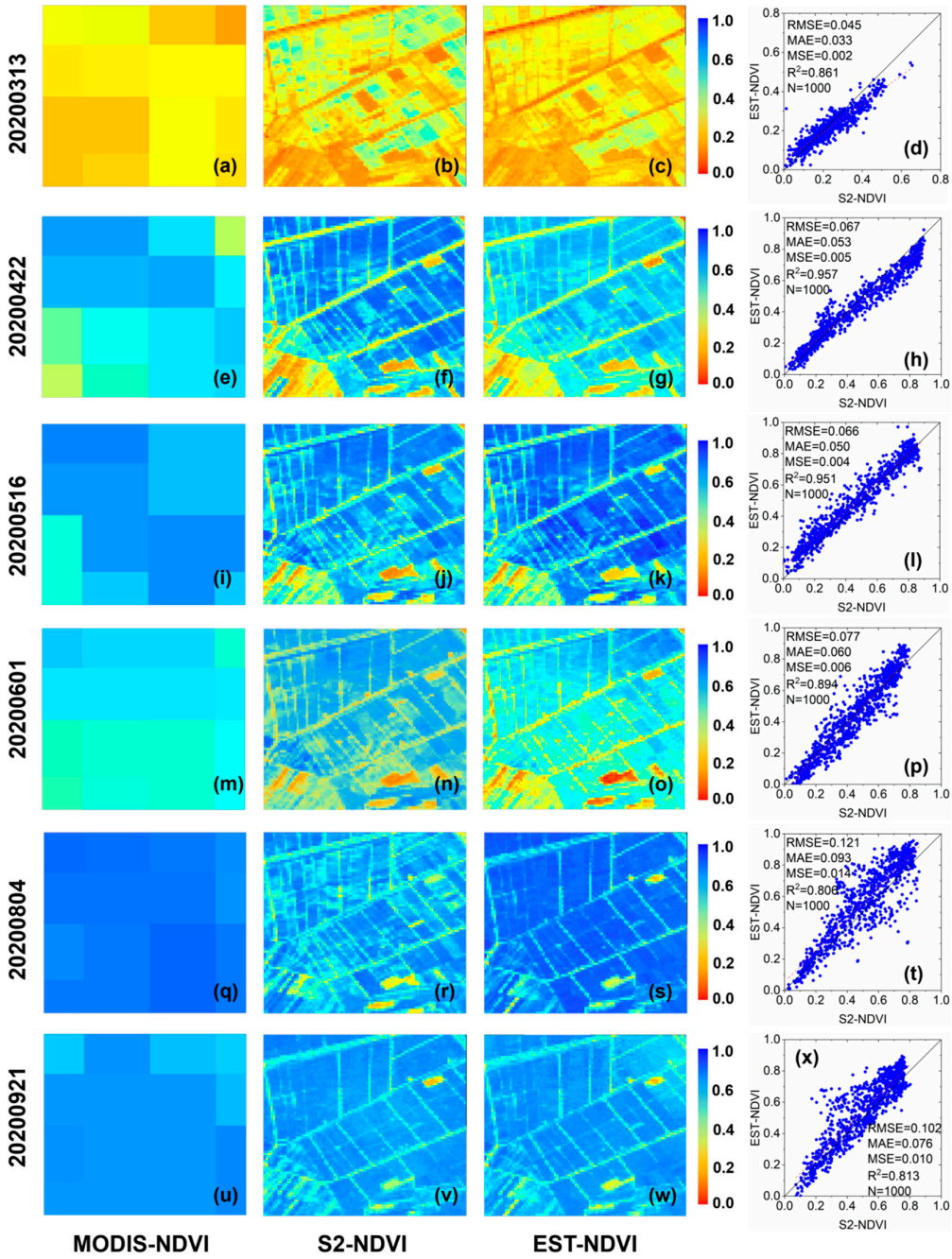


Figure 5. Spatial distribution of multi-source NDVI (MODIS-NDVI, S2-NDVI, and EST-NDVI) in a 1 km × 1 km sub-region of Area 1 on selected dates in 2020. The scatter plots show the relationship between S2-NDVI and EST-NDVI pixel values, with statistical metrics indicating the accuracy of the fusion process. Subfigures (**a**–**d**), (**e**–**h**), (**i**–**l**), (**m**–**p**), (**q**–**t**), and (**u**–**x**) represent the MODIS-NDVI, S2-NDVI, EST-NDVI, and the corresponding validation scatter plots for the dates of 13 March, 22 April, 16 May, 1 June, 4 August, and 21 September 2020, respectively.

3.2. Comparison of σ^0_{soil} and σ^0

The relationship between the linear and decibel values of the σ^0 is expressed as $y = e^{0.2303x}$ [39]. The linear value of σ^0_{soil} ranges from 0 to 1. Scatter plots were generated using data from all monitoring stations in Area 1, covering the period from 1 January 2020 to 15 July 2021, with a total of 531 data points. Figure 6 shows the σ^0_{soil} values for different polarization modes. For VV polarization, the σ^0 values (in db) range from −18 db to 4 db, with an average of −11.012 db. The linear value range after exponential transformation is 0–0.35, with an average value of 0.089. In VH polarization, the σ^0 (db) is between −30 db and −12 db, with an average value of −18.701 db. The linear value range after exponential transformation is 0–0.06, with an average value of 0.017. At the same time, it is found that the σ^0 of VV polarization is larger than that of VH polarization, and both the linear and decibel values are similar to those reported by Ouaadi et al. [40].

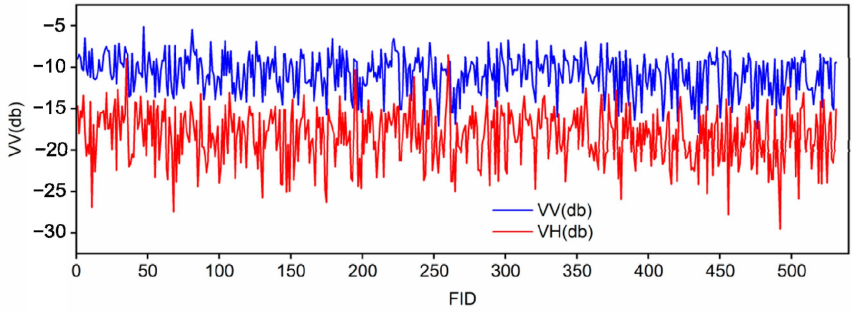


Figure 6. The σ^0_{soil} for different polarization modes. Blue represents VV polarization and red represents VH polarization.

3.3. Establishment and Validation of SSM Estimation Models

3.3.1. Establishment and Validation of SSM Estimation Models for Different Land Uses

Figure 7 illustrates the scatter plots of the SSM estimation models under various polarization models and land use types. The models were developed based on the σ^0_{soil} and in situ SSM. The results indicate that VV polarization exhibits greater sensitivity to soil reflection signals, resulting in significantly higher estimation accuracy compared to VH polarization. The dataset comprises 531 observations, encompassing cropland, forest, and grassland land use types. The established SSM estimation models include the model in multiple land use combinations (Multiple-Model), the model in cropland (Cropland-Model), the model in forest (Forest-Model), and the model in grassland (Grassland-Model) in VV and VH polarization. The number of the in situ SSM used for the establishment of Cropland-Model, Forest-Model, and Grassland-Model are 297, 181, and 53, respectively. These in situ SSMs are the sum of effective points accumulated by all dates in Area 1 (Figure 1) from 1 January 2020 to 15 July 2021, which are the same as the S1 transit date. Among them, the in situ SSM in cropland was more than half, accounting for 55.9%, mainly because the SM sites were mainly distributed in cropland. As shown in Figure 7, among the Multiple-Model, Cropland-Model, Forest-Model, and Grassland-Model, the estimation accuracy of the models in VV polarization is higher than that of VH polarization. The R^2 of Multiple-Model, Cropland-Model, Forest-Model, and Grassland-Model is 0.622, 0.599, 0.626, and 0.637 higher than that of the models in VH polarization, respectively. This is similar to the conclusion of Bao et al. [27]. However, their research object is herbaceous plants, and our study is mainly aimed at the cropland. In VV and VH polarization, the estimation accuracy of the Grassland-Model is the best (VV: MSE = 0.002, RMSE = 0.043, MAE = 0.032, R^2 = 0.839; VH: MSE = 0.011, RMSE = 0.103, MAE = 0.085, R^2 = 0.202). This may be due to the smaller size of grassland plants and the smaller influence of grassland plants on soil reflection signals. Studies have shown that the WCM is suitable for SSM estimation in low

vegetated areas [25]. The Forest-Model has the worst estimation accuracy (VV: MSE = 0.005, RMSE = 0.068, MAE = 0.059, and R^2 = 0.731; VH: MSE = 0.019, RMSE = 0.138, MAE = 0.126, and R^2 = 0.105). This may be due to the high vegetation height of forest and the greater effect of forest on the soil reflection signal. Furthermore, there may be limitations to these conclusions. In the process of establishing the model, the number of SSM measurements for different land uses was inconsistent, and the number of SSM measurements in the grassland was only 53. In future studies, the number of SSM measurements in all land uses should be consistent as far as possible.

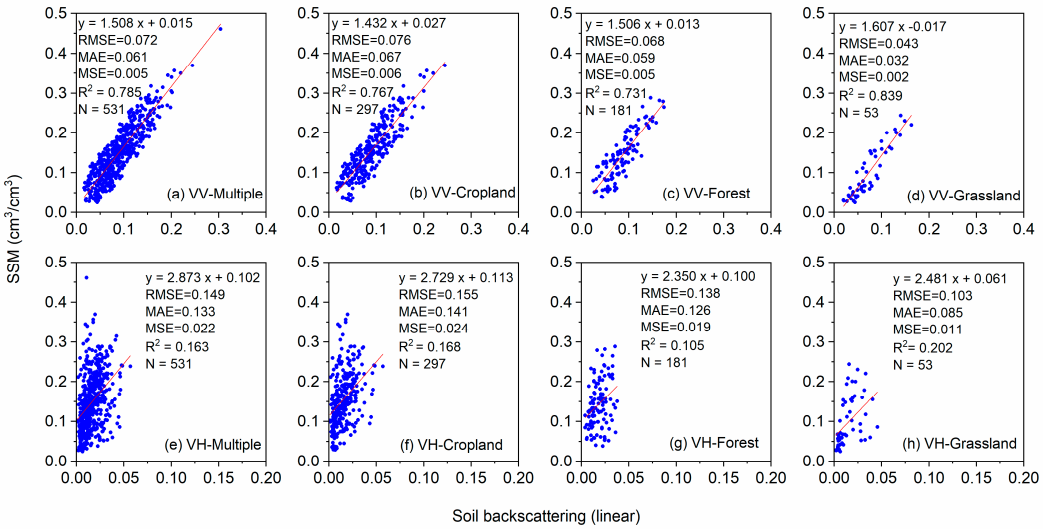


Figure 7. SSM estimation model under different polarization modes and different land use types. The first row is VV polarization, and the second row is VH polarization. The first column is multiple land use combinations, the second column is farmland, the third column is forest, and the fourth column is grassland.

This study focuses on cropland and provides scientific guidance for agricultural irrigation and agricultural water management. Therefore, only the Multiple-Model and Cropland-Model were verified. The validation data are derived from the measured SSM of all dates from 1 January 2020 to 15 July 2021 in Area 2 (Figure 1), which are the same as S1 transit dates. The validation results of VV polarization are better than those of VH polarization. It is recommended to use the model in VV polarization for SSM estimation in the Haihe basin. The estimation accuracy difference between the Multiple-Model and the Cropland-Model is small.

In VV polarization, the R^2 of the Multiple-Model is higher than that of the Cropland-Model (Multiple-Model: R^2 = 0.891; Cropland-Model: R^2 = 0.886). However, the RMSE and MAE of the Multiple-Model are smaller than those of the Cropland-Model (Multiple-Model: RMSE = 0.024 cm^3/cm^3, MAE = 0.019 cm^3/cm^3; Cropland-Model: RMSE = 0.023 cm^3/cm^3, MAE = 0.018 cm^3/cm^3). Therefore, the backscattering in VV polarization is more suitable for SSM estimation. When multiple land uses are mixed, model ($y = 0.977x + 0.007$) is recommended (Figure 8a). For the cropland, model ($y = 0.889x + 0.024$) is recommended (Figure 8b).

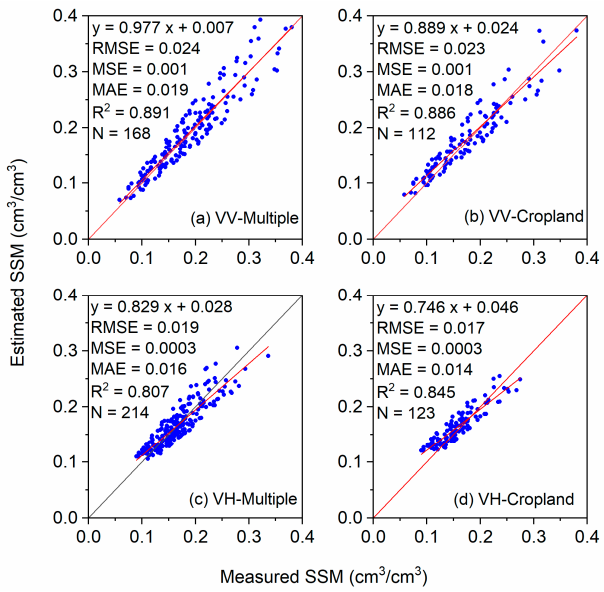


Figure 8. Estimated SSM over the validation site "Area 2" from the entire database (multiple land use combinations and cropland) in different polarizations.

3.3.2. Establishment and Validation of SSM Estimation Models in Different FVC Intervals

SSM modeling was performed on different FVC intervals of the multiple land use combinations and the cropland, and 16 models were verified by the in situ SSM. The corresponding names of each FVC interval are $0 < FVC < 0.45$, low coverage; $0.45 \leq FVC < 0.6$, middle coverage; $0.6 \leq FVC < 0.75$, mid-high coverage; and $0.75 \leq FVC < 1$, high coverage [38]. Figures 9 and 10 show the vegetation coverage interval models in VV polarization and VH polarization, respectively. The R^2 in VV polarization, ranging from 0.714 to 0.808, is higher than that in VH polarization, which ranges from 0.026 to 0.272.

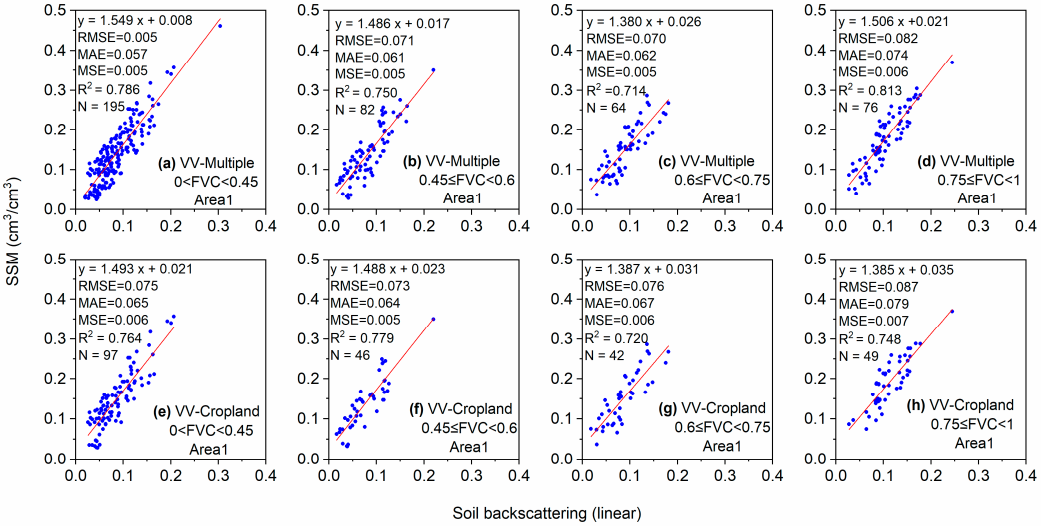


Figure 9. The SSM estimation model under different FVC intervals in VV polarization: (**a**) VV-Multiple with low coverage; (**b**) VV-Multiple with middle coverage; (**c**) VV-Multiple with mid-high coverage; (**d**) VV-Multiple with high coverage; (**e**) VV-Cropland with low coverage; (**f**) VV-Cropland with middle coverage; (**g**) VV-Cropland with mid-high coverage; (**h**) VV-Cropland with high coverage.

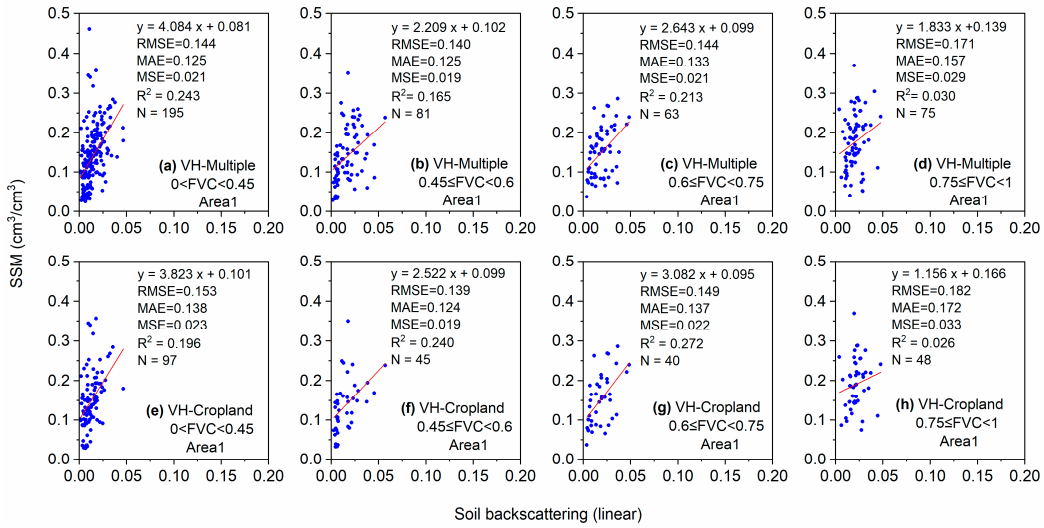


Figure 10. SSM estimation model under different FVC intervals in VH polarization: (**a**) VH-Multiple with low coverage; (**b**) VH-Multiple with middle coverage; (**c**) VH-Multiple with mid-high coverage; (**d**) VH-Multiple with high coverage; (**e**) VH-Cropland with low coverage; (**f**) VH-Cropland with middle coverage; (**g**) VH-Cropland with mid-high coverage; (**h**) VH-Cropland with high coverage.

In VH polarization, the R^2 of the Multiple-Model at low coverage and high coverage is higher than that of Cropland-Model, and the R^2 of the Multiple-Model at middle coverage and mid-high coverage is lower than that of the Cropland-Model. In VV polarization, the R^2 of the Multiple-Model at high coverage is higher than that of the Cropland-Model, and the R^2 of the Multiple-Model at low coverage, middle coverage, and mid-high coverage is lower than that of Cropland-Model. In general, the gap in R^2 between the Multiple-Model and the Cropland-Model of each FVC interval is small.

Section 3.3.1 has shown that the R^2 of the model in VV polarization is higher, and the validation results are better than VH polarization. In addition, the different FVC interval models described above also show that the R^2 of the models at VV polarization is higher. Therefore, this section exclusively validates the model using VV polarization, generating scatter plots to depict the validation outcomes. Figure 11 presents the validation results of the SSM estimation models across various FVC intervals. The findings indicate a notable decline in estimation accuracy when FVC surpasses 0.75. This reduction in accuracy is likely attributable to the dense vegetation canopy, which attenuates microwave signal penetration to the soil surface, thereby complicating the precise estimation of SSM in areas with high vegetation density. The RMSE, MSE, MAE, and R^2 of the Multiple-Model were 0.024–0.055 cm^3/cm^3, 0.0006–0.013 cm^3/cm^3, 0.018–0.039 cm^3/cm^3, and 0.411–0.904, respectively. The RMSE, MSE, MAE and R^2 of the Cropland-Model were 0.023–0.063 cm^3/cm^3, 0.0005–0.0039 cm^3/cm^3, 0.017–0.051 cm^3/cm^3, and 0.358–0.924, respectively. In both the Multiple-Model and the Cropland-Model, R^2 decreases with the increase in FVC. When FVC $\geq$ 0.6, R^2 decreases to a lower value (Multiple-Model: R^2 = 0.488; Cropland-Model: R^2 = 0.396). When FVC $\geq$ 0.75, R^2 reaches the lowest value (Multiple-Model: R^2 = 0.411; Cropland-Model: R^2 = 0.358), RMSE and MAE reach the maximum value (Multiple-Model: RMSE = 0.055 cm^3/cm^3, MAE = 0.039 cm^3/cm^3; Cropland-Model: RMSE = 0.063 cm^3/cm^3, MAE = 0.051 cm^3/cm^3). It can be seen that the WCM is not suitable for SSM estimation when FVC $\geq$ 0.6. In this case, the vegetation layer is relatively dense, and only few microwave signals may be detected.

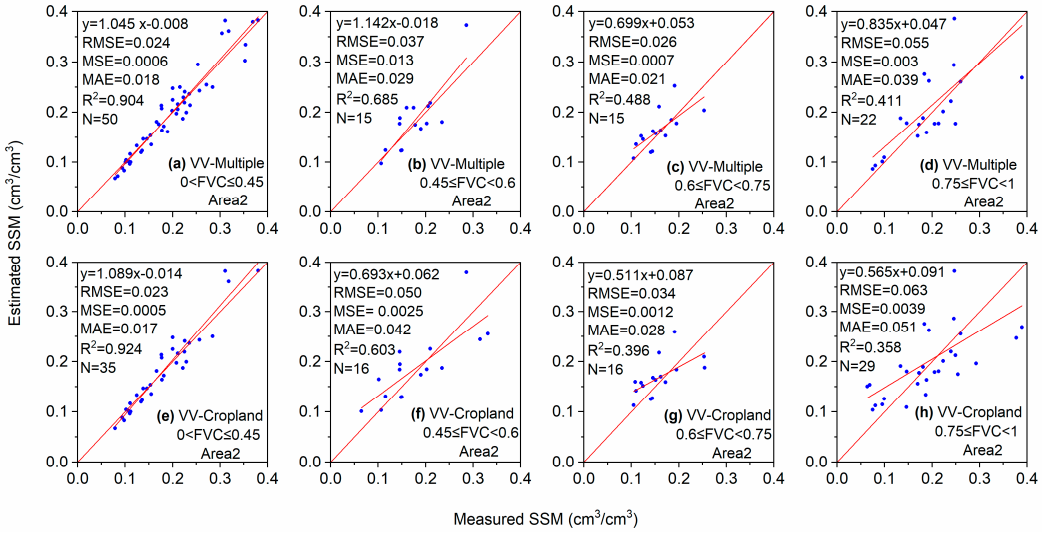


Figure 11. Estimated SSM over the validation site "Area 2" from the entire database (multiple land use combinations and cropland) in VV polarization: (**a**) VV-Multiple with low coverage; (**b**) VV-Multiple with middle coverage; (**c**) VV-Multiple with mid-high coverage; (**d**) VV-Multiple with high coverage; (**e**) VV-Cropland with low coverage; (**f**) VV-Cropland with middle coverage; (**g**) VV-Cropland with mid-high coverage; (**h**) VV-Cropland with high coverage.

3.4. Spatial Distribution of SSM

Figure 12 shows the spatial distribution of SSM during the winter wheat growing season in Handan, Haihe Basin. The SSM values are higher in the eastern region, which is characterized by lower elevation and more intensive agricultural activities. This pattern is consistent with the higher irrigation rates typically applied in these areas during the early stages of wheat production. The lower SSM in the western region, with higher elevation, suggests less irrigation and potentially different land management practices. The SSM in cropland was obtained by cutting the SSM results with the cropland vector data. The Cropland-Model in VV polarization in Section 3.3.1 is used. The elevation of Handan is characterized by high in the west and low in the east. The SSM of the 8 days was between 0 and 0.53 cm^3/cm^3. The SSM in the western was small, mostly between 0 and 0.22 cm^3/cm^3, and the SSM in the eastern was large, mostly greater than 0.24 cm^3/cm^3. The mean values of SSM on 10 March, 22 March, 3 April, 15 April, 27 April, 9 May, 21 May, and 2 June 2020 were 0.29, 0.29, 0.28, 0.29, 0.28, 0.23, 0.25, and 0.26 cm^3/cm^3, respectively, and the standard deviations were 0.052, 0.056, 0.060, 0.056, 0.065, 0.062, 0.055, and 0.057 cm^3/cm^3, respectively. The main crop planted in Handan is wheat, and March and April are the initial stages of wheat production. More irrigation times and irrigation amount are the main reasons for the large SSM. This provides scientific support for regional agricultural irrigation and agricultural water management.

Figure 13 shows the spatial distribution of SSM in the growing season of summer maize in Handan, Haihe Basin, with a total of 8 days (14 June, 26 June, 8 July, 20 July, 1 August, 13 August, 25 August, 6 September 2020). The SSM in cropland was obtained by cutting the SSM results with the cropland vector data. The Cropland-Model in VV polarization in Section 3.3.1 is used. The SSM of the eight days was between 0 and 0.53 cm^3/cm^3. From June to September, the main crop planted in Handan is summer maize. The mean values of SSM on 14 June, 26 June, 8 July, 20 July, 1 August, 13 August, 25 August, and 6 September 2020 were 0.24, 0.22, 0.23, 0.22, 0.23, 0.21, 0.21, and 0.22 cm^3/cm^3, respectively, and the standard deviations were 0.051, 0.047, 0.046, 0.044, 0.044, 0.046, 0.044, and 0.044 cm^3/cm^3, respectively. The variation in SSM during the growing season of summer maize was small,

which was related to crop growth characteristics. Summer corn is not irrigated except in the early sowing period.

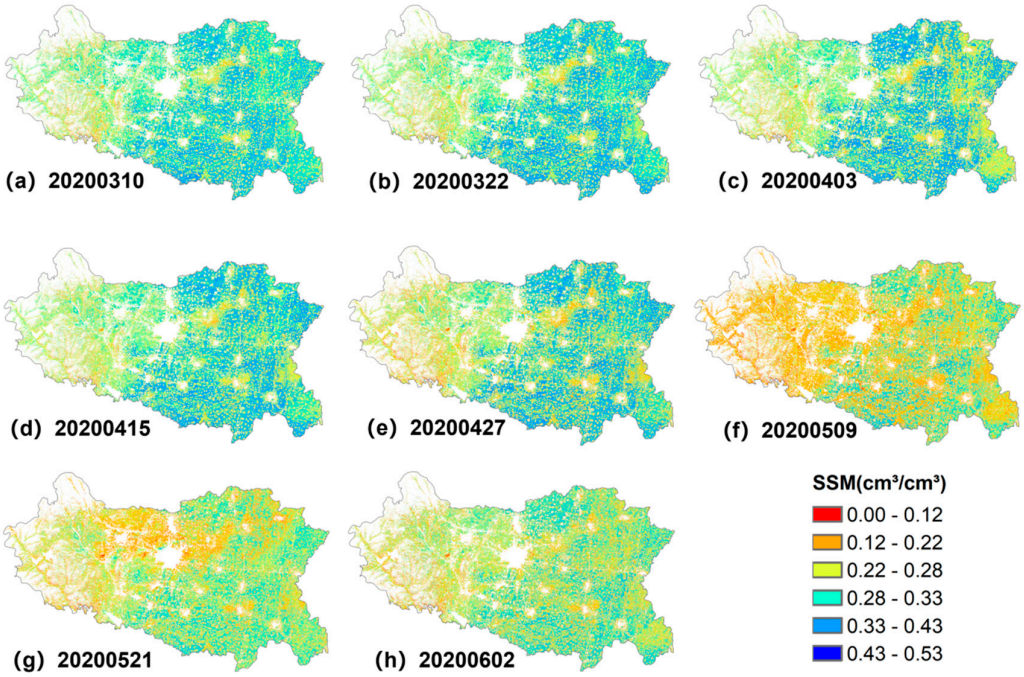


Figure 12. Spatial distribution of SSM in the winter wheat growing season in Handan, Haihe Basin.

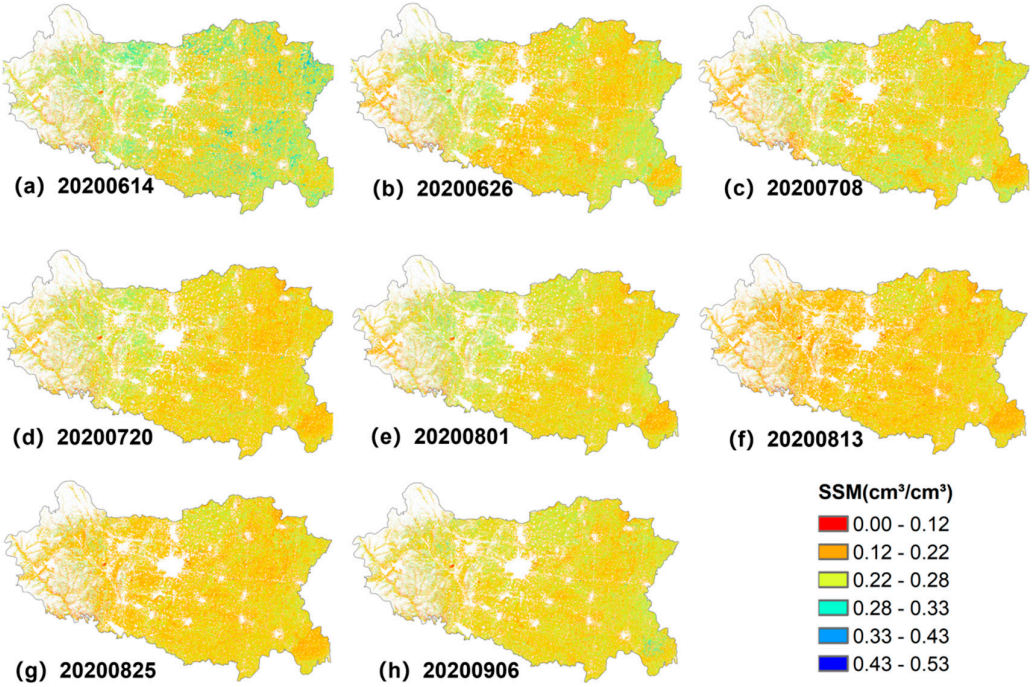


Figure 13. Spatial distribution of SSM in the summer maize growing season in Handan, Haihe Basin.

The findings of this study highlight the importance of considering vegetation cover and land use when estimating SSM using microwave RS. The results suggest that the WCM is particularly effective in cropland areas with moderate vegetation cover (FVC $\leq$ 0.75), providing valuable insights for optimizing agricultural irrigation practices and improving water resource management in the Haihe Basin.

4. Discussion

4.1. Comparison with the Previous Studies and Model Performance

The Multiple-Model and Cropland-Model both showed high estimation accuracy, with R^2 values of 0.891 and 0.886, respectively. This indicates the models are robust and can be effectively applied to estimate SSM in the Haihe Basin. However, the lower R^2 values in high FVC intervals (FVC > 0.75) suggest that the WCM may not be suitable for areas with dense vegetation cover, where alternative models or additional data sources may be required. In this study, the NDVI was used to characterize the VWC [41], the VWC was substituted into the WCM, and then SSM was estimated. At the same time, the SSM estimation accuracy under different land use types and FVC intervals was studied. The estimation accuracy of the Multiple-Model and Cropland-Model is satisfactory (Multiple-Model: RMSE = 0.024 cm^3/cm^3, MSE = 0.001 cm^3/cm^3, MAE = 0.019 cm^3/cm^3, R^2 = 0.891; Cropland-Model: RMSE = 0.023 cm^3/cm^3, MSE = 0.001 cm^3/cm^3, MAE = 0.018 cm^3/cm^3, R^2 = 0.886). As the VWC is one of the important parameters of the WCM, the estimation accuracy of the VWC directly affects the estimation accuracy of SSM, so many scholars [28,42,43] have extensively researched screening the optimal vegetation index to estimate the VWC. Common vegetation indexes include the MCARI, NDWI, and NDVI. Compared with similar studies, this study improves the availability and matching degree of the NDVI, and effectively improves the estimation accuracy of SSM. Lin et al. [25] estimated the VWC by the MCARI, and estimated SSM in Daxing and Gu'an, China, based on the improved WCM. The estimation accuracy (RMSE = 0.028 cm^3/cm^3, MAE = 0.023 cm^3/cm^3, R^2 = 0.867) is lower than that in this study (RMSE = 0.024 cm^3/cm^3, MAE = 0.019 cm^3/cm^3, R^2 = 0.891). This improvement may be attributed to the use of the ESTARFM, which increases the temporal resolution of the NDVI and improves the matching degree between the NDVI and σ_{soil}. However, the linear relationship between σ_{soil} and SSM, while practical, may oversimplify the complex interactions among SM, surface roughness, and vegetation effects. Non-linear models or machine learning methods (e.g., PIML-SM, PINN-SM) could potentially capture these interactions more accurately. Future studies should explore these alternative formulations to improve the robustness of SSM estimation under diverse environmental conditions. Of course, it may also be the deviation caused by inconsistent modeling and validation samples. Bao et al. [27] used the NDWI to estimate the VWC, and then estimated SSM for Spain and UK based on the improved WCM. The R^2 and RMSE were calculated as 0.81 and 0.053 cm^3/cm^3, respectively. Zeng et al. [44] also used the combination of VV polarization and the NDVI to estimate SSM based on the support vector machine (SVM). The R^2 of the model is high, but the RMSE is large, and the validation accuracy is not high overall (R^2 = 0.842, RMSE = 2.071 cm^3/cm^3). Before the results reported herein, scholars may have thought there was a large gap in the accuracy of models established with different land uses. The accuracy difference between the Multiple-Model and the Cropland-Model, however, is found to be small. This may be due to the difference between microwave signals and optical RS satellite signals—microwave wavelength is longer, the penetration ability is stronger, and the microwave is not sensitive to the land use. Therefore, in VV polarization, the validation accuracy gap between the Multiple-Model and the Cropland-Model is small. The microwave signal is more sensitive to the FVC. Although the microwave penetration ability is strong, when the FVC exceeds a certain value, the part of the microwave signal reaching the soil will be greatly reduced, so the stability of the model is poor. When the FVC > 0.6, the estimation accuracy of SSM is found to decrease significantly. In the future, it may be necessary to consider or develop other models to estimate the cropland SSM at a regional scale with high FVC.

The results of this study have significant implications for water resource management and agricultural practices in the Haihe basin. The high accuracy of SSM estimation in

croplands can help farmers optimize irrigation schedules, particularly during critical growth stages of crops such as wheat and maize. By providing timely and accurate SSM data, our model can support precision agriculture, reducing water waste and improving crop yields. During the early growth stages (March to April), winter wheat requires sufficient SM to ensure proper germination and root development. Our model can help farmers monitor SSM levels and schedule irrigation to avoid water stress, which can significantly impact crop yield. In the later stages of summer maize growth (July to September), SSM monitoring can help farmers avoid excessive irrigation, which not only wastes water but can also lead to waterlogging and nutrient leaching. By integrating SSM data into irrigation management systems, farmers can achieve more efficient water use, reducing water waste and improving crop productivity. This is particularly important in the Haihe basin, where water resources are limited and agricultural water demand is high.

For water resource management, the ability to monitor SSM at a regional scale can aid in the allocation of water resources, especially in areas with limited water availability. Policymakers can use the SSM to develop more efficient irrigation policies and water distribution plans, ensuring sustainable water use. Water managers can use the SSM maps generated by our model to identify areas with low SSM levels and prioritize water allocation to these regions. This can help ensure that water resources are distributed more equitably and efficiently across the basin. SSM is an important variable in agricultural drought monitoring and forecasting [45]. The ability to monitor SSM in near real-time can also aid in drought early-warning systems. By identifying areas with declining SM levels, water managers can take proactive measures to mitigate the impacts of drought, such as implementing water-saving measures or providing emergency water supplies to affected areas.

4.2. Limitations of the ESTARFM Fusion Process and Sensitivity Analysis

The ESTARFM method effectively improves the temporal and spatial resolution of the NDVI, but it is not without limitations. The fusion process is highly sensitive to prolonged cloud cover, which can lead to data gaps and inconsistencies in temporal sampling [46]. In regions with frequent cloud cover, the availability of high-quality optical data (e.g., S2) may be limited, potentially affecting the accuracy of the fused NDVI. Additionally, the fusion process may introduce uncertainties due to the interpolation of missing data, which could propagate into the subsequent SSM estimation. Future studies should consider incorporating error propagation analysis to quantify how uncertainties in the fused NDVI affect the final SSM estimates.

The vegetation attenuation coefficients (A and B) were calibrated based on the main crops in the Haihe Basin (summer maize and winter wheat). While these parameters were chosen to minimize error during the calibration process, their robustness across different vegetation types and conditions remains to be fully explored. Sensitivity analysis should be conducted to assess how variations in A and B affect the model's performance. This would provide insights into the model's applicability in regions with different vegetation characteristics.

Additionally, the influence of surface roughness on SSM estimation was not considered in this study. Surface roughness can significantly affect the backscattering coefficient, and ignoring this factor may lead to errors in SSM estimation. Future research should incorporate surface roughness parameters into the model to improve estimation accuracy, especially in areas with complex terrain. Instead, the two sub-study areas were considered to be flat overall, and the influence of surface roughness was ignored. In this study, the σ^0 received by the microwave sensor is equal to the sum of the σ^0_{veg} and σ^0_{soil}, and the surface roughness is regarded as a constant. The σ^0_{soil} is not only closely related to SSM, but also

affected by surface roughness [47–49]. Ma et al. [50] considered the surface roughness to improve the WCM, and estimated cropland SSM in Spain. The results showed the precision of the improved WCM is better than the WCM. The improved WCM can effectively establish the relationship between the σ^0 and SSM, improve the estimation accuracy of SSM, and provide research ideas for SSM estimation in other land uses.

Due to the limited penetration capability of the C-band sensor on S1, it cannot detect the root zone soil signal, so only the SSM estimation model is proposed in this study. However, root zone SM is an important variable in hydrological and climate prediction models, which can affect surface soil evaporation and vegetation transpiration, and thus regulate the soil–vegetation–atmosphere water and energy balance [51]. Therefore, the next step should focus on how to estimate root zone SM. Chen et al. [52] carried out the simulation of root zone SM at site scale in the Weishan Irrigation District based on data assimilation, and the simulation results were satisfactory (RMSE, 0.02–0.07 cm^3/cm^3; MAE, 0.06–0.20 cm^3/cm^3). And the application of data assimilation technology can reduce the error by 30–50%. Cheng et al. [53] used multi-source RS data to calculate multiple vegetation indices, and estimated SM at 10, 20, 40, 60, and 80 cm depth based on machine learning. The estimation of SM at multiple depths was realized, and the accuracy was good (R^2, 0.72–0.8; RMSE, 0.09–0.13 cm^3/cm^3), but the spatial distribution information of root zone SM was not obtained.

4.3. Impact of Polarization and Vegetation Cover on SSM Estimation

This study found that VV polarization yields higher sensitivity and better SSM estimation accuracy compared to VH polarization. This difference can be attributed to the dual behavior of VH polarization, which is influenced by both soil and vegetation backscattering. VV polarization, on the other hand, is more sensitive to SM due to its stronger interaction with the soil surface. Future studies could explore the use of additional polarization modes (e.g., HH, HV) or complementary sensors (e.g., L-band SAR) to mitigate the limitations observed in VH polarization and improve SSM estimation in densely vegetated areas.

The model's performance degrades significantly when FVC exceeds 0.75, primarily due to the dense vegetation layer attenuating microwave signals and reducing their penetration to the soil surface. To address this limitation, future studies could explore the integration of additional vegetation indices (e.g., NDWI, EVI) or non-linear corrections to improve SSM estimation in high FVC conditions. For instance, the use of multi-angle or multi-frequency SAR data could enhance the model's ability to penetrate dense vegetation and provide more accurate SSM estimates.

4.4. Error Analysis, Uncertainty Analysis, and Spatial Distribution Analysis

To provide a more comprehensive understanding of the reliability and robustness of the SSM estimation model, this section delves into a detailed error analysis, uncertainty analysis, and spatial distribution analysis. These analyses are critical for assessing the model's performance under different environmental conditions and for identifying potential sources of error that may affect the accuracy of SSM estimates.

4.4.1. Error Analysis

The error analysis focuses on quantifying the discrepancies between the model-estimated SSM and the in situ measurements. The primary metrics used for error analysis include the RMSE, MAE, and R^2. These metrics provide a quantitative assessment of the model's accuracy and its ability to capture the spatial and temporal variability of SSM.

RMSE measures the average magnitude of the errors between the estimated and observed SSM values. In this study, the RMSE values for the Multiple-Model and Cropland-Model were 0.024 cm^3/cm^3 and 0.023 cm^3/cm^3, respectively, indicating a high level of

accuracy. However, the RMSE increased significantly in high FVC intervals (FVC $\geq$ 0.75), reaching 0.055 cm^3/cm^3 for the Multiple-Model and 0.063 cm^3/cm^3 for the Cropland-Model. This suggests that the model's performance degrades in densely vegetated areas, likely due to the attenuation of microwave signals by the vegetation layer. MAE provides a measure of the average absolute deviation between the estimated and observed SSM values. The MAE for the Multiple-Model and Cropland-Model was 0.019 cm^3/cm^3 and 0.018 cm^3/cm^3, respectively, indicating that the model's estimates are generally close to the observed values. However, similar to RMSE, the MAE increased in high FVC intervals, reaching 0.039 cm^3/cm^3 for the Multiple-Model and 0.051 cm^3/cm^3 for the Cropland-Model. This further underscores the challenges posed by dense vegetation in accurately estimating SSM. R^2 measures the proportion of the variance in the observed SSM that is explained by the model. The R^2 for the Multiple-Model and Cropland-Model was 0.891 and 0.886, respectively, indicating a strong correlation between the estimated and observed SSM values. However, the R^2 decreased significantly in high FVC intervals, dropping to 0.411 for the Multiple-Model and 0.358 for the Cropland-Model. This highlights the limitations of the model in densely vegetated areas, where the penetration of microwave signals to the soil surface is significantly reduced.

4.4.2. Uncertainty Analysis

The ESTARFM used to fuse MODIS and S2 NDVI introduces uncertainties due to the interpolation of missing data, particularly in regions with prolonged cloud cover. These uncertainties can propagate into the SSM estimation process, affecting the accuracy of the final SSM estimates. To quantify this uncertainty, we conducted a sensitivity analysis by varying the input parameters of the ESTARFM and assessing the impact on the fused NDVI and subsequent SSM estimates. The results indicate that the uncertainty in the fused NDVI can lead to variations in the SSM estimates, particularly in regions with inconsistent temporal sampling.

The vegetation attenuation coefficients (A and B) used in the WCM were calibrated based on the main crops in the Haihe Basin. However, these parameters may not be robust across different vegetation types and environmental conditions. To assess the sensitivity of the model to these parameters, in the future, we can conduct a Monte Carlo simulation by varying A and B within a reasonable range and evaluating the impact on the SSM estimates.

The in situ SSM measurements used for model validation are subject to measurement errors, which can affect the accuracy of the validation results. To quantify this uncertainty, we conducted a bootstrap analysis by resampling the in situ SSM data and assessing the variability in the validation metrics (RMSE, MAE, and R^2). The results indicate that the measurement uncertainty can lead to variations in the validation metrics, particularly in regions with sparse in situ measurements.

4.4.3. Spatial Distribution Analysis

The spatial distribution analysis focuses on assessing the spatial variability of the SSM estimates and identifying regions where the model's performance may be limited. The spatial distribution of SSM in the Haihe Basin was analyzed for different land use types and FVC intervals. The results indicate that the SSM estimates are generally accurate in croplands with moderate vegetation cover (FVC $\leq$ 0.75), but the accuracy decreases significantly in densely vegetated areas (FVC > 0.75) and regions with complex terrain.

The SSM estimates in croplands were highly accurate, with RMSE values ranging from 0.023 cm^3/cm^3 to 0.063 cm^3/cm^3, depending on the FVC interval. The spatial distribution of SSM in croplands was consistent with the observed irrigation patterns, with higher SSM values in regions with more intensive agricultural activities. The SSM estimates in

forests and grasslands were less accurate, particularly in densely vegetated areas. The RMSEs in these regions were significantly higher, reaching 0.138 cm^3/cm^3 for forests and 0.103 cm^3/cm^3 for grasslands. This is likely due to the limited penetration of microwave signals in densely vegetated areas, which reduces the model's ability to accurately estimate SSM. The SSM estimates in regions with complex terrain were also less accurate, particularly in areas with significant microtopography. This is likely due to the assumption of constant surface roughness in the WCM, which may not hold in regions with varying terrain. Future studies should consider incorporating surface roughness parameters into the model to improve the accuracy of SSM estimates in complex terrains.

5. Conclusions

In this study, we used the ESTARFM to obtain the NDVI with high temporal and spatial resolution, and estimated SSM using the WCM. Our results demonstrate that VV polarization is more sensitive to soil reflection signals, providing higher accuracy in SSM estimation. The model performed well in croplands, with no significant difference in accuracy between the Multiple-Model and the Cropland-Model. However, the model is not suitable for SSM estimation in forested areas, and its accuracy decreases when FVC exceeds 0.75. The findings of this study have important implications for agricultural irrigation and water resource management in the Haihe basin. By providing accurate SSM estimates, our model can help farmers optimize irrigation practices and improve water use efficiency. For future research, we recommend exploring the integration of multi-source remote sensing data to improve SSM estimation in high vegetation cover areas. Additionally, future studies should focus on estimating root zone SM, which is crucial for understanding the soil–vegetation–atmosphere water balance.

Author Contributions: Methodology, R.L.; data processing, Z.H. and X.Z. (Xinyu Zhao); data analysis and validation, R.L. and Z.H.; funding acquisition, X.X.; project administration, X.Z. (Xiaohua Xu); proofreading, G.W. and Y.S.; review and editing, H.S. All authors have read and agreed to the published version of the manuscript.

Funding: This research was funded by the Key Research and Development Project of Jiangxi Province (20232BBG70029), the Technology Innovation Guidance Program of Jiangxi Province (2023KSG01005), the Science and Technology Project of Jiangxi Provincial Water Resources Department (202426ZDKT18), the Project of Jiangxi Natural Science Foundation (20202BABL204068), the Science and Technology Project of Jiangxi Provincial Water Resources Department (202425YBKT19), the Student Innovation and Entrepreneurship Training Program Projects (S202311319006, 202411319004), and the Key Research and Development Project of Jiangxi Province (20223AEI91008).

Institutional Review Board Statement: Not applicable.

Data Availability Statement: The data presented in this study are available on request from the first author (R.L.).

Acknowledgments: We would like to thank the anonymous reviewers for their long-term guidance and constructive comments.

Conflicts of Interest: The authors declare no conflicts of interest.

References

1. Zhu, P.; Jia, X.; Zhao, C.; Shao, M. Long-term soil moisture evolution and its driving factors across China's agroecosystems. *Agric. Water Manag.* **2022**, *269*, 107735. [CrossRef]
2. Shu, F.; Wenwu, Z.; Liding, C.; Nan, L. Advances in landscape ecology in the Loess Plateau since 2010 in China. *Acta Ecol. Sin.* **2017**, *37*, 3957–3966. [CrossRef]
3. Lu, A.; Shuyi, S.; Shuguang, L.; Hongzhang, M. Research progress on the cooperative inversion of soil moisture using optical and SAR remote sensing. *Remote Sens. Nat. Resour.* **2021**, *33*, 10–18. [CrossRef]

4. Jain, S. A Comparative Study of Oven Drying Method and Microstrip Moisture Sensor for Determination of Moisture Content of Soil and Analysis of Bulking of Sand Phenomenon. *Wirel. Pers. Commun.* **2024**, *139*, 1659–1667. [CrossRef]
5. Dong, H.H.; Chen, Y.M.; Li, Y.C. Mini time domain reflectometry probe for monitoring local soil moisture of cut-off walls in centrifuge model tests. *Transp. Geotech.* **2024**, *47*, 101278. [CrossRef]
6. Bai, L.; Long, D.; Yan, L. Estimation of Surface Soil Moisture With Downscaled Land Surface Temperatures Using a Data Fusion Approach for Heterogeneous Agricultural Land. *Water Resour. Res.* **2019**, *55*, 1105–1128. [CrossRef]
7. Zhao, Y.; Zhang, X.; Bai, Y.; Mi, F. Does Land Use Change Affect Green Space Water Use? An Analysis of the Haihe River Basin. *Forests* **2019**, *10*, 545. [CrossRef]
8. Nagaraju, S.K.T.; Pathak, A.A. Retrieving Surface and Rootzone Soil Moisture Using Microwave Remote Sensing. *J. Indian Soc. Remote Sens.* **2024**, *52*, 1415–1430. [CrossRef]
9. Jackson, R.D.; Idso, S.B.; Reginato, R.J.; Pinter, P.J., Jr. Canopy temperature as a crop water stress indicator. *Water Resour. Res.* **1981**, *17*, 1133–1138. [CrossRef]
10. Hernández-López, J.A.; Andrade, H.J.; Barrios, M. Agricultural drought assessment in dry zones of Tolima, Colombia, using an approach based on water balance and vegetation water stress. *Sci. Total Environ.* **2024**, *921*, 171144. [CrossRef]
11. Liu, G.S.; Tian, S.K.; Wang, Q.; Wang, H.Z.; Kong, L.W. High-resolution measurement of moisture filed at soil surface with interfered image processing method and machine learning techniques. *J. Hydrol.* **2025**, *652*, 132623. [CrossRef]
12. Lin, R.; Chen, H.; Zhang, D.; Wei, Z.; Cai, J.; Zeng, R.; Zhang, L.; Jia, Y. Estimating Topsoil Water Content Using Crop Water Stress Index and Remote Sensing Technologies. *J. Irrig. Drain.* **2023**, *42*, 1–7. [CrossRef]
13. Yadav, M.; Vashisht, B.B.; Vullaganti, N.; Kumar, P.; Jalota, S.K.; Kumar, A.; Kaushik, P. UAV-enabled approaches for irrigation scheduling and water body characterization. *Agric. Water Manag.* **2024**, *304*, 109091. [CrossRef]
14. Guan, Y.Y.; Grote, K. Assessing the Potential of UAV-Based Multispectral and Thermal Data to Estimate Soil Water Content Using Geophysical Methods. *Remote Sens.* **2024**, *16*, 61. [CrossRef]
15. Vahidi, M.; Shafian, S.; Thomas, S.; Maguire, R. Pasture Biomass Estimation Using Ultra-High-Resolution RGB UAVs Images and Deep Learning. *Remote Sens.* **2023**, *15*, 5714. [CrossRef]
16. Balenzano, A.; Mattia, F.; Satalino, G.; Davidson, M.W.J. Dense Temporal Series of C- and L-band SAR Data for Soil Moisture Retrieval Over Agricultural Crops. *IEEE J. Sel. Top. Appl. Earth Obs. Remote Sens.* **2011**, *4*, 439–450. [CrossRef]
17. Attema, E.P.W.; Ulaby, F.T. Vegetation modeled as a water cloud. *Radio Sci.* **1978**, *13*, 357–364. [CrossRef]
18. Ulaby, F.T.; Dubois, P.C.; Zyl, J.V. Radar mapping of surface soil moisture. *J. Hydrol.* **1996**, *184*, 57–84. [CrossRef]
19. Kumar, K.; Suryanarayana Rao, H.P.; Arora, M.K. Study of water cloud model vegetation descriptors in estimating soil moisture in Solani catchment. *Hydrol. Process.* **2015**, *29*, 2137–2148. [CrossRef]
20. Zribi, M.; Kotti, F.; Amri, R.; Wagner, W.; Shabou, M.; Lili-Chabaane, Z.; Baghdadi, N. Soil moisture mapping in a semiarid region, based on ASAR/Wide Swath satellite data. *Water Resour. Res.* **2014**, *50*, 823–835. [CrossRef]
21. Han, D.; Yang, H.; Qiu, C.; Yang, G.; Chen, E.; Du, Y.; Yang, W.; Zhou, C. Estimating wheat biomass from GF-3 data and a polarized water cloud model. *Remote Sens. Lett.* **2018**, *10*, 234–243. [CrossRef]
22. Bai, X.; He, B. Potential of Dubois model for soil moisture retrieval in prairie areas using SAR and optical data. *Int. J. Remote Sens.* **2015**, *36*, 5737–5753. [CrossRef]
23. Gherboudj, I.; Magagi, R.; Berg, A.A.; Toth, B. Soil moisture retrieval over agricultural fields from multi-polarized and multi-angular RADARSAT-2 SAR data. *Remote Sens. Environ.* **2011**, *115*, 33–43. [CrossRef]
24. Hosseini, M.; McNairn, H. Using multi-polarization C- and L-band synthetic aperture radar to estimate biomass and soil moisture of wheat fields. *Int. J. Appl. Earth Obs. Geoinf.* **2017**, *58*, 50–64. [CrossRef]
25. Lin, R.; Chen, H.; Wei, Z.; Li, Y.; Zhang, B.; Sun, H.; Cheng, M. Improved Surface Soil Moisture Estimation Model in Semi-Arid Regions Using the Vegetation Red-Edge Band Sensitive to Plant Growth. *Atmosphere* **2022**, *13*, 930. [CrossRef]
26. Zhang, L.; Meng, Q.; Yao, S.; Wang, Q.; Zeng, J.; Zhao, S.; Ma, J. Soil Moisture Retrieval from the Chinese GF-3 Satellite and Optical Data over Agricultural Fields. *Sensors* **2018**, *18*, 2675. [CrossRef]
27. Bao, Y.; Lin, L.; Wu, S.; Kwal Deng, K.A.; Petropoulos, G.P. Surface soil moisture retrievals over partially vegetated areas from the synergy of Sentinel-1 and Landsat 8 data using a modified water-cloud model. *Int. J. Appl. Earth Obs. Geoinf.* **2018**, *72*, 76–85. [CrossRef]
28. Baghdadi, N.; El Hajj, M.; Zribi, M.; Bousbih, S. Calibration of the Water Cloud Model at C-Band for Winter Crop Fields and Grasslands. *Remote Sens.* **2017**, *9*, 969. [CrossRef]
29. Gong, P.; Chen, B.; Li, X.; Liu, H.; Wang, J.; Bai, Y.; Chen, J.; Chen, X.; Fang, L.; Feng, S.; et al. Mapping essential urban land use categories in China (EULUC-China): Preliminary results for 2018. *Sci. Bull.* **2020**, *65*, 182–187. [CrossRef]
30. Amazirh, A.; Merlin, O.; Er-Raki, S.; Gao, Q.; Rivalland, V.; Malbeteau, Y.; Khabba, S.; Escorihuela, M.J. Retrieving surface soil moisture at high spatio-temporal resolution from a synergy between Sentinel-1 radar and Landsat thermal data: A study case over bare soil. *Remote Sens. Environ.* **2018**, *211*, 321–337. [CrossRef]

31. Peng, Z.; Yong, L. An Interpolation Method for Stripe Missing in the Product MOD09A1. *Remote Sens. Technol. Appl.* **2015**, *30*, 331–336. [CrossRef]
32. Zhu, X.; Chen, J.; Gao, F.; Chen, X.; Masek, J.G. An enhanced spatial and temporal adaptive reflectance fusion model for complex heterogeneous regions. *Remote Sens. Environ.* **2010**, *114*, 2610–2623. [CrossRef]
33. Bai, L.; Cai, J.; Liu, Y.; Chen, H.; Zhang, B.; Huang, L. Responses of field evapotranspiration to the changes of cropping pattern and groundwater depth in large irrigation district of Yellow River basin. *Agric. Water Manag.* **2017**, *188*, 1–11. [CrossRef]
34. Bindlish, R.; Barros, A.P. Parameterization of vegetation backscatter in radar-based, soil moisture estimation. *Remote Sens. Environ.* **2001**, *76*, 130–137. [CrossRef]
35. Kong, J.; Yang, J.; Zhen, P.; Li, J.; Yang, L. A Coupling Model for Soil Moisture Retrieval in Sparse Vegetation Covered Areas Based on Microwave and Optical Remote Sensing Data. *IEEE Trans. Geosci. Remote Sens.* **2018**, *56*, 7162–7173. [CrossRef]
36. Mattia, F.; Satalino, G.; Dente, L.; Pasquariello, G. Using a priori information to improve soil moisture retrieval from ENVISAT ASAR AP data in semiarid regions. *IEEE Trans. Geosci. Remote Sens.* **2006**, *44*, 900–912. [CrossRef]
37. Gutman, G.; Ignatov, A. The derivation of the green vegetation fraction from NOAA/AVHRR data for use in numerical weather prediction models. *Int. J. Remote Sens.* **2010**, *19*, 1533–1543. [CrossRef]
38. Lin, W.; Na, L.; Guangchao, W.; Yunhang, Y. Vegetation Coverage Changes and Driving Forces in He'nan Section of Yellow River Basin. *Bull. Soil Water Conserv.* **2022**, *42*, 393–399. [CrossRef]
39. Nguyen, H.H.; Cho, S.; Choi, M. Spatial soil moisture estimation in agro-pastoral transitional zone based on synergistic use of SAR and optical-thermal satellite images. *Agric. For. Meteorol.* **2022**, *312*, 108719. [CrossRef]
40. Ouaadi, N.; Jarlan, L.; Ezzahar, J.; Zribi, M.; Khabba, S.; Bouras, E.; Bousbih, S.; Frison, P.-L. Monitoring of wheat crops using the backscattering coefficient and the interferometric coherence derived from Sentinel-1 in semi-arid areas. *Remote Sens. Environ.* **2020**, *251*, 112050. [CrossRef]
41. Jackson, T.J.; Vine, D.M.L.; Hsu, A.Y.; Oldak, A.; Starks, P.J.; Swift, C.T.; Isham, J.D.; Haken, M. Soil moisture mapping at regional scales using microwave radiometry: The Southern Great Plains Hydrology Experiment. *IEEE Trans. Geosci. Remote Sens.* **2008**, *37*, 2136–2151. [CrossRef]
42. El Hajj, M.; Baghdadi, N.; Zribi, M.; Bazzi, H. Synergic Use of Sentinel-1 and Sentinel-2 Images for Operational Soil Moisture Mapping at High Spatial Resolution over Agricultural Areas. *Remote Sens.* **2017**, *9*, 1292. [CrossRef]
43. Prakash, R.; Singh, D.; Pathak, N.P. A Fusion Approach to Retrieve Soil Moisture With SAR and Optical Data. *IEEE J. Sel. Top. Appl. Earth Obs. Remote Sens.* **2012**, *5*, 196–206. [CrossRef]
44. Zeng, X.; Xing, Y.; Shan, E.; Zhang, Y.; Wang, C. Soil water content retrieval based on Sentinel-1A and Landsat 8 image for Bei'an-Heihe Expressway. *Chin. J. Eco-Agric.* **2017**, *25*, 118–126. [CrossRef]
45. Luan, Q.H.; Gu, P.C.; Sun, Q.Y.; Lai, B.; Zhou, Y.L.; Weng, B.S. Agricultural drought evaluation based on a soil moisture index coupled hydrological model in North China Plain. *Ecol. Indic.* **2024**, *166*, 112473. [CrossRef]
46. Guo, H.; Wang, X.; Ouyang, Z.; Chen, S.; Che, T.; Zheng, Z. Application of the ESTARFM algorithm for fusing Sentinel-2 and MODIS NDSI series in the eastern Qilian Mountains. *J. Hydrol. Reg. Stud.* **2025**, *57*, 102103. [CrossRef]
47. Oh, Y.; Kay, Y.C. Condition for precise measurement of soil surface roughness. *IEEE Trans. Geosci. Remote Sens.* **1998**, *36*, 691–695. [CrossRef]
48. Periasamy, S. Significance of dual polarimetric synthetic aperture radar in biomass retrieval: An attempt on Sentinel-1. *Remote Sens. Environ.* **2018**, *217*, 537–549. [CrossRef]
49. Srivastava, H.S.; Patel, P.; Manchanda, M.L.; Adiga, S. Use of multiincidence angle RADARSAT-1 SAR data to incorporate the effect of surface roughness in soil moisture estimation. *IEEE Trans. Geosci. Remote Sens.* **2003**, *41*, 1638–1640. [CrossRef]
50. Ma, T.; Han, L.; Liu, Q. Inversion of surface soil moisture content of Spanish farmland using modified water cloud model. *Trans. Chin. Soc. Agric. Eng.* **2019**, *35*, 129–135. [CrossRef]
51. Bouyssel, F.; Calvet, J.-C.; Jarlan, L.; Sabater, J.M.; De Rosnay, P. From Near-Surface to Root-Zone Soil Moisture Using Different Assimilation Techniques. *J. Hydrometeorol.* **2007**, *8*, 194–206. [CrossRef]
52. Chen, H.; Lin, R.; Zhang, B.; Wei, Z. Improving Soil Water Content and Surface Flux Estimation Based on Data Assimilation Technique. *Remote Sens.* **2022**, *14*, 3183. [CrossRef]
53. Cheng, M.; Li, B.; Jiao, X.; Huang, X.; Fan, H.; Lin, R.; Liu, K. Using multimodal remote sensing data to estimate regional-scale soil moisture content: A case study of Beijing, China. *Agric. Water Manag.* **2022**, *260*, 107298. [CrossRef]

Disclaimer/Publisher's Note: The statements, opinions and data contained in all publications are solely those of the individual author(s) and contributor(s) and not of MDPI and/or the editor(s). MDPI and/or the editor(s) disclaim responsibility for any injury to people or property resulting from any ideas, methods, instructions or products referred to in the content.